Journal of *Marine Science and Engineering*

MDPI

Article

Analysis of Flow Instability and Mechanical Energy Loss of Fluid Field in Fluid Momentum Wheel

Kedong Zhang [1], Wenhua Wang [1,*], Yihua Liu [1], Linlin Wang [2], Yazhen Du [2], Hongxia Li [1] and Yi Huang [1,*]

[1] School of Naval Architecture, Dalian University of Technology, Dalian 116024, China
[2] Tianjin Navigation Instruments Research Institute, Tianjin 300131, China
* Correspondence: wangwenhua@dlut.edu.cn (W.W.); huangyi@dlut.edu.cn (Y.H.)

Abstract: A new type of anti-rolling device denoted as a fluid momentum wheel (FMW) is proposed to address the limitations of traditional gyrostabilizers in reducing the roll responses of floating platforms in waves. The proposed device is based on the same gyroscope theorem, which differs from a rigid gyrostabilizer in that the internal fluid generates secondary flow in the cross-section under the combined effects of inertial centrifugal force and a radial pressure gradient, and the streamwise velocity exhibits a non-uniform distribution. These instability phenomena may cause mechanical energy loss in the flow field, which is critical for selecting the driving device and the anti-roll control performance of offshore platforms. In the study, different turbulence models are compared with the results of a Direct Numerical Simulation (DNS) and experiments to ensure the accuracy of the numerical method, and the spatiotemporal distribution characteristics of the flow field in FMW are analyzed. Therein, the SST k-ω model accurately verifies the flow instability phenomenon of the FMW observed in the Particle Image Velocimetry (PIV) experiment. Next, this paper proposes corresponding evaluation parameters to assess the impact of typical parameters on the flow field instability. The results show that the flow instability increases with an increase in the typical parameters of FMWs (such as the pipe diameter, curvature radius, and velocity). Furthermore, the paper discusses the relationship between dimensionless mechanical factors (Reynolds number, curvature ratio) and the spatiotemporal instability of the flow field, revealing the essential effects of the curvature ratio and Reynolds number on the loss coefficient.

Keywords: fluid momentum wheel; turbulence models; flow instability; mechanical energy loss; dimensionless mechanical factors

Citation: Zhang, K.; Wang, W.; Liu, Y.; Wang, L.; Du, Y.; Li, H.; Huang, Y. Analysis of Flow Instability and Mechanical Energy Loss of Fluid Field in Fluid Momentum Wheel. *J. Mar. Sci. Eng.* **2024**, *12*, 331. https://doi.org/10.3390/jmse12020331

Academic Editor: Pietro Scandura

Received: 12 January 2024
Revised: 5 February 2024
Accepted: 9 February 2024
Published: 15 February 2024

1. Introduction

In complex sea conditions, the environmental loads, such as wind, waves, and currents, inevitably lead to the roll and pitch motion responses of ships and floating platforms [1–3], affecting the regular operation of equipment and causing safety risks to personnel. Therefore, it is necessary to choose appropriate anti-roll methods to ensure the motion stability of ships and platforms under load disturbances.

Currently, the widely used anti-roll devices mainly include bilge keels, fin stabilizers, anti-roll tanks, gyrostabilizers, and so on [4–8]. Among these, gyrostabilizers employ the gyroscope theorem to obtain amplified precession output torque, effectively suppressing roll motion. Moreover, gyrostabilizers are known for their easy installation, small space requirements, and ability to achieve excellent anti-rolling performance even at zero speed [9]. Therefore, gyrostabilizers have emerged as a promising and highly regarded solution for reducing roll, captivating the attention of both the international academic and industry communities [10–14]. Based on the same principle, the Fluid Momentum Wheel (FMW) has special structural features that provide high safety and stability. Besides their anti-roll function, FMW can also be used for ballasting or adjusting the center of gravity, presenting extensive prospects for application. Arranging the FMW underwater offers advantages

in terms of the release and replenishment of fluid medium and heat dissipation [15]. The concept of FMW and its potential advantages in satellite and ship applications was first proposed by Maynard [16], laying the foundation for the design of the FMW and providing a clear direction for further research. In 2004, the Texas University Fluid Loop Orientation/Attitude Test (FLOAT) team [17] developed and tested a fluid momentum controller consisting of multiple water-filled loops driven by mechanical pumps and underwent ground and flight tests to assess the attitude-control capability. Extensive research has been conducted on the application of the FMW in the aerospace industry, specifically for satellite attitude control.

However, there has been limited exploration and systematic investigation of the application of FMW devices in ocean engineering. As a new type of anti-roll measure, the related research contents and key problems of the FMW are extensive. Du et al. [18] designed a stable offshore platform based on toroidal flow with the principle of angular momentum, demonstrating its ability to resist roll and pitch motion responses. Additionally, Wang et al. [19] analyzed the flow characteristics of the FMW through a PIV experiment and numerical simulation and confirmed its gyroscopic precession characteristics. These findings indicate that the enclosed volume of the FMW can be easily increased, which means that greater anti-roll performance can be achieved. Compared to traditional rigid gyrostabilizers, FMW utilizes a fluid medium to generate the angular momentum, and thus, the stability of the flow field may significantly affect fluid resistance and the anti-roll effect.

Under the combined effect of centrifugal force and a radial pressure gradient, curved pipes generate a pair of counter-rotating vortices within the plane known as Dean Vortices by Dean [20], which results in the non-uniform distribution of streamwise fluid velocities across the cross-section. This phenomenon is believed to cause higher fluid resistance compared to straight pipes under similar flow velocities, based on the studies on flow phenomena and mechanical energy loss in various curved pipes [21–24]. White [25] was one of the earliest researchers to conduct experimental studies on pressure loss in helical pipes, and the results were in good agreement with the earlier theoretical work by Dean [20]. Ito [26] conducted experimental research on pressure loss in toroidal pipes with flowing water, establishing a correlation between the friction factor and the Dean number. El-Genk and Schriener [27] comprehensively summarized experimental data on pressure loss and convective heat transfer in toroidal and helical pipes, revealing that secondary flows can enhance convective heat transfer while simultaneously increasing pressure loss. Existing studies indicate that the loss factors in curved pipes rely on not only the Reynolds number but also geometric parameters (such as bend angle, radius of curvature, inlet-outlet area ratio, and so on).

In addition, scholars have also conducted some studies on the flow phenomena and instability of curved pipes [24,28,29]. Sudo et al. [30] conducted experimental studies on flow separation phenomena in a 90° bend and analyzed the variation in secondary flow in the downstream flow field through the physical quantity of the swirl intensity of secondary flow. The research by Kim et al. [31] further revealed a strong correlation between the swirl intensity of secondary flow and the curvature radius of a 90° bend while showing a weak correlation with the Reynolds number. Recently, some researchers [32–35] employed the PIV measurement technique to study the flow field and turbulence structure in curved pipes. Among them, Ikarashi et al. [32] investigated the influence of bend curvature (1.0, 1.2, 1.5) on the flow field of a 90° bend, specifically analyzing the phenomena of flow separation and secondary flow. It was observed that flow separation occurred on the inner wall near the bend exit, particularly at smaller radius ratios, increasing the velocity of the secondary flow and turbulent kinetic energy. Noorani et al. [36,37] employed the Direct Numerical Simulation (DNS) method to simulate fully developed flow in toroidal pipes with varying curvatures and Reynolds numbers, aiming to analyze the swirl-switching phenomenon of secondary flow. In another study, Wegt et al. [38] employed the Large Eddy Simulation (LES) method to analyze the variations in the position of the vortex core and the distribution of streamwise velocity downstream of a 90° bend. He et al. [39] used LES and

the Proper Orthogonal Decomposition (POD) method to study the correlation between the secondary flow motion and wall shear stress in 90° bends at different Reynolds numbers (5300, 27,000, and 45,000). Until now, most studies on flow fields and energy losses in curved pipes focus on common configurations, such as 90° bends and U-shaped pipes with inlets and outlets. Due to the enclosed circular structure of the FMW, the relevant research data are limited. The secondary flow and streamwise velocity stratification inside the FMW induce changes in flow instability, resulting in differences in energy losses. A further quantitative evaluation of flow instability is necessary to explore its inherent relationship with energy losses.

The paper can be organized as follows. Section 2 compares different turbulence models with DNS results and then analyzes the phenomena of in-plane secondary flow and the non-uniform distribution of streamwise velocities in the spatial, as well as temporal, pulsation characteristics in the FMW. Section 3 establishes evaluation parameters to study the influence of typical parameters of the FMW (for example, pipe diameter, curvature radius, velocity) on the spatiotemporal instability of the flow field. Furthermore, dimensionless mechanical factors of the Reynolds number and curvature ratio are presented to analyze the characteristics of flow instability and quantify its influence on energy losses. Finally, concluding remarks and future perspectives are presented in Section 4.

2. Numerical Methods and Validation

This study employed the STAR-CCM+ 2022.1.1 software based on the finite volume method to solve the governing equations with the second-order discrete scheme in both time integration and spatial discretization. The chosen time resolution ensured that the Courant number should be less than 1 throughout the entire computational domain, and the y^+ values can satisfy the requirements of the selected turbulence model. The research subject is a unique toroidal pipe that exhibits a closed geometric structure without explicit import/export boundaries. In order to simulate the fully developed flow, periodic boundary conditions were applied at the inlet and outlet with the source term of the pressure gradient in the streamwise direction to balance the fluid resistance, and no-slip conditions were imposed on the wall surfaces, as shown in Figure 1a. The cylindrical coordinate system takes the geometric center of the toroidal pipe as the origin, and the circumferential direction (θ) represents the streamwise direction. The mesh generation for the cross-section of a pipe was arranged with an "O-grid" to make the mesh distribution more uniform and the transition smoother. The circular cross-section is discretized by five blocks, with one block located in the center of the pipe and the other four blocks surrounding the pipe to achieve its circular shape, as shown in Figure 1b. The coordinate system is established as a cylindrical coordinate system with the geometric center of the pipe cross-section as the origin, and the vertical direction (s) represents the streamwise direction. The selection of mesh parameters for the pipe has been validated in the previous study.

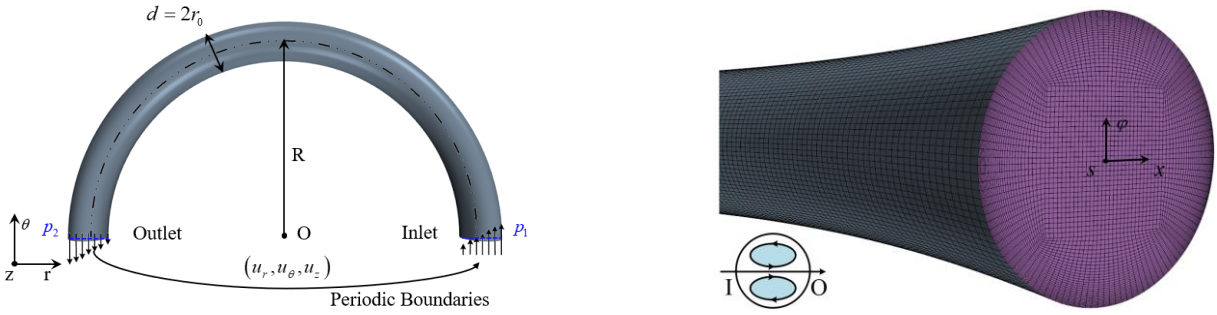

(**a**) Geometric model (**b**) Grid structure

Figure 1. Schematic of geometric model and grid structure. (I is the inside and O is the outside.)

The fluid medium investigated in this paper is water, and the turbulent state of the curved pipe is considered to be three-dimensional, incompressible, and viscous without

heat exchange. In order to analyze the turbulent flow, each variable in the instantaneous Navier-Stokes equations is separated into its mean value and fluctuating value, which is given by $\Phi = \varphi + \varphi'$. Therein, Φ can denote the velocity and pressure, and the fluctuating mass force is neglected. The governing equations are the unsteady three-dimensional, incompressible Reynolds-averaged Navier-Stokes (RANS) equations, which include the following mass and momentum conservation equations:

$$\frac{\partial u_i}{\partial x_i} = 0 \tag{1}$$

$$\frac{\partial u_i}{\partial t} + u_j \frac{\partial u_i}{\partial x_j} = f_i - \frac{1}{\rho}\frac{\partial p}{\partial x_i} + \frac{\partial}{\partial x_j}\left(\nu \frac{\partial u_i}{\partial x_j} - {u'}_i {u'}_j\right) \tag{2}$$

Compared to the traditional N-S equations, the Reynolds-averaged equation has an additional Reynolds stress term, which represents the influence of turbulent fluctuations on the time-averaged flow. In order to solve the Reynolds-averaged equations, numerical simulation methods can be divided into direct numerical simulation (DNS) and non-direct numerical simulation. DNS directly solves the instantaneous turbulent governing equations, while non-direct numerical simulation approximates and simplifies turbulent characteristics to solve the Reynolds stress, which can be further categorized into Large Eddy Simulation (LES) and Reynolds-Averaged Navier-Stokes (RANS) methods. Among them, DNS requires no simplifications or approximations for turbulent flow and can provide accurate results with errors mainly from numerical computations. LES assumes that turbulent fluctuations and mixing are primarily caused by large-scale vortices in the flow field, which derive energy from the mean flow and exhibit substantial anisotropy. Therefore, for large-scale vortex motions that can be captured by the grid, the fluctuation terms can be calculated directly by solving the governing equations. For small vortices that cannot be captured, the subgrid-scale model is employed to simulate the impact of small-scale vortex motions on large-scale motions, and the Dynamic Smagorinsky subgrid-scale model of LES was employed in this study. Furthermore, in order to solve the Reynolds-averaged equation, the RANS method makes some assumptions about the Reynolds stress, which involves establishing stress expressions or introducing new turbulence models that relate the Reynolds stress to the time-averaged quantities. The Reynolds Stress Transport (RST) model calculates the components of the Reynolds stress tensor by solving the transport equations. The pressure-strain term in the Reynolds stress transport equation was calculated by employing the Elliptic Blending (EB) model in this study. Moreover, according to the Boussinesq assumption, the Reynolds stress is a function of the turbulent eddy viscosity μ_t and can be expressed as Equation (3).

$$-\rho u_i' u_j' = 2\mu_t s_{ij} - \frac{2}{3}\rho k \delta_{ij} \tag{3}$$

where δ_{ij} is the Kronecker delta, and s_{ij} is the average strain tensor. The standard k-ε model is one of the most fundamental two-equation models, which introduces the turbulent kinetic energy (k) and the dissipation rate (ε) equations, respectively. Additionally, there are other models, such as the standard k-ω model and the SST k-ω model. The SST k-ω model, proposed by Menter [40], is a hybrid model that combines the advantages of the standard k-ε and k-ω models. The SST k-ω model is more suitable for studying the flow field in curved pipes due to its combination of the favorable properties of the k-ω model for low-Reynolds-number flow near the wall and the k-ε model for far-field calculations. The turbulent eddy viscosity in this model is defined by the following:

$$\mu_t = \rho k T \tag{4}$$

$$T = \min\left(\frac{a^*}{\omega}, \frac{a_1}{SF_2}\right) \tag{5}$$

$$F_2 = \tanh\left(\left(\max\left(\frac{2\sqrt{k}}{\beta^*\omega d}, \frac{500\mu}{\rho d^2\omega}\right)\right)^2\right) \quad (6)$$

where S is the modulus of the average strain tensor, a^* and β^* are model coefficients, a_1 is 0.31, and d is the distance from the wall.

In order to validate the accuracy of the numerical method, the computed results obtained from different turbulence models were compared with DNS results. The models adopted the same parameters as DNS, including the curvature ratio (r_0/R) of 0.1 and Reynolds number of 11,700 [36]. The Fanning friction factor (f) and the computational costs were taken into consideration for evaluating the analysis validity.

$$f = \overline{\tau}_\theta / \left(\rho {u_b}^2/2\right) \quad (7)$$

where τ_θ denotes the streamwise component of the mean wall shear stress, an overbar denotes the average value along the circumference of the pipe section, and u_b is the bulk velocity.

From the results in Table 1, it can be observed that the Realizable k-ε model demonstrates a larger discrepancy in predicting the friction factor (f) compared to other turbulence models, which is consistent with the findings in the study of Noorani et al. [36]. The study indicated that while the k-ε model can predict turbulence in straight pipes and mildly curved pipes, it exhibits significant deviations in cases with high curvature. Considering computational efficiency, the SST k-ω model is undoubtedly the best choice.

Table 1. Results and computational efficiency of different turbulence models.

Turbulence Models	DNS	LES	RST	SST k-ω	Realizable k-ε
Fanning friction factor (f)	0.0094	0.0092	0.0097	0.0096	0.0108
Relative error	/	−1.61%	3.91%	2.81%	15.34%
Computational costs (CPU)	/	42 cores × 48 h	42 cores × 12 h	22 cores × 8 h	22 cores × 6 h

Assuming the rotor of the rigid-body gyrostabilizer is identical to the FMW, the rotational angular velocities of the rotor are the same. As depicted in Figure 2a, the rotor velocity increases radially from the inside to the outside, with a normalized velocity range of 0.9~1.1. Figure 2b,c present the transient flow fields of DNS and LES in the cross-section of the FMW. Due to the influence of fluid viscosity, the velocity at the wall is zero, and the range of velocity fluctuations expands to 0~1.5. Additionally, both velocities exhibit strong fluctuation characteristics due to the influence of turbulent eddies, which are generated near the wall and subsequently develop, affecting the flow field at the center. Consequently, this gives rise to the first unstable phenomenon of the FMW compared to the gyrostabilizer, namely the fluid velocity fluctuations.

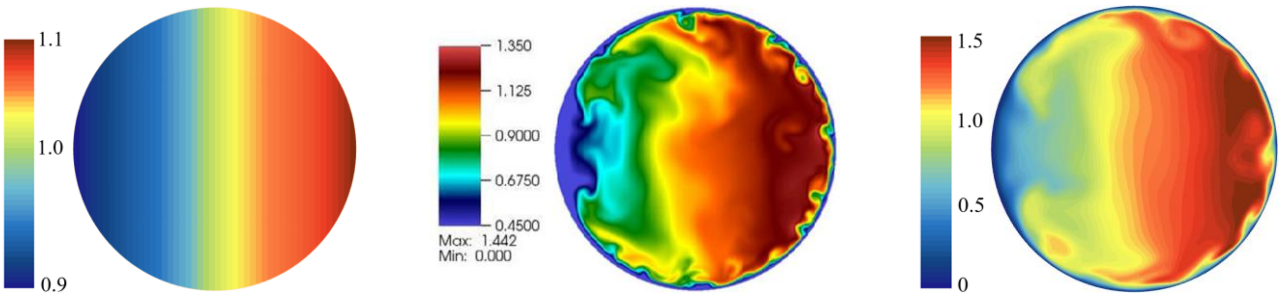

(**a**) Rigid-body gyrostabilizer (**b**) DNS (**c**) LES

Figure 2. Normalized velocity profiles of rigid-body gyrostabilizer and FMW.

The average flow field, which can show the spatial distribution characteristic, can be obtained by averaging time on the instantaneous fluid field. Figure 3 compares the average flow fields in the DNS and LES cross-section with the RANS method results, including the RST model, the SST k-ω model, and the Realizable k-ε model. The normalized velocities in the plane ($\sqrt{u_r{}^2 + u_z{}^2}/u_b$) and in the streamwise direction (u_θ/u_b) represent the upper and lower sides of the figure, respectively. From the velocity distribution in the streamwise direction for DNS and other models, it can be observed that under the action of inertial centrifugal force, regions with higher velocities tend to be located towards the outer side, while lower velocities are found on the inner side, presenting the phenomenon of velocity stratification similar to that of the rigid-body gyrostabilizer. In the presence of an imbalance between inertial centrifugal force and the radial pressure gradient, the secondary flow phenomenon is observed in the plane of the FMW. The velocity profile on the upper plane clearly demonstrates that LES and SST k-ω models provide a closer approximation to the DNS results than other models. The in-plane velocities are primarily concentrated near the upper wall, while the counter-rotating vortices with an outward shift are observed near the inner side. In contrast, the backflow effect of the secondary flow near the inner wall is weak in the RST model, resulting in significant deviations from the DNS results. The Realizable k-ε model overestimates the influence of inertial centrifugal force, resulting in a greater outward shift and an expanded range of influence from the secondary flow. Therefore, regarding the velocity distribution in the flow field of the FMW, LES and the SST k-ω model demonstrate better similarity to the DNS results.

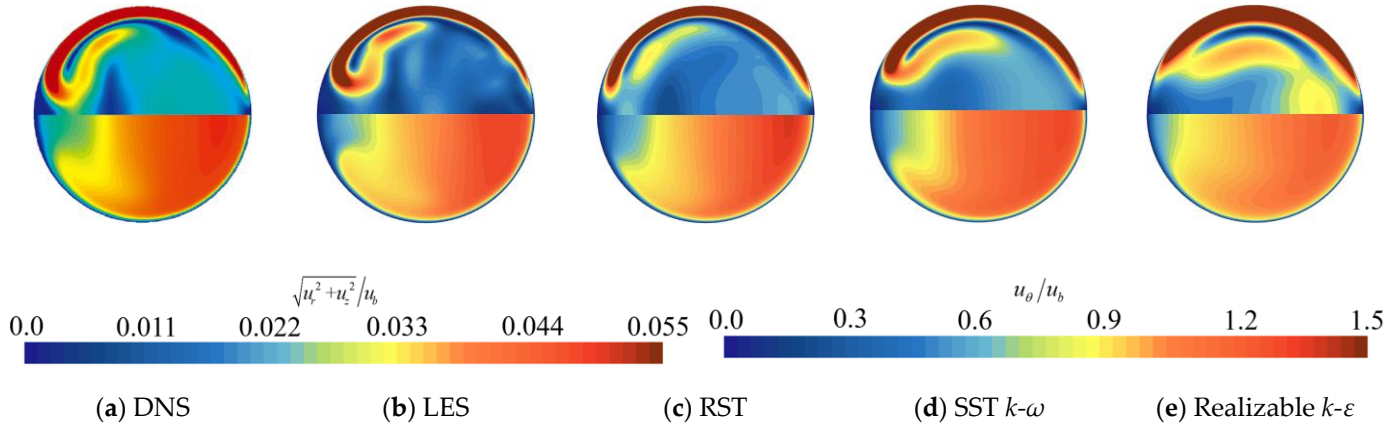

(**a**) DNS (**b**) LES (**c**) RST (**d**) SST k-ω (**e**) Realizable k-ε

Figure 3. Spatial distribution characteristics of different turbulence models: normalized time-averaged flow field in the plane (upper side) and streamwise direction (lower side).

Turbulent kinetic energy is commonly used to quantify the intensity of velocity fluctuations and describe the temporal characteristics of the flow field. Figure 4 presents the distribution of normalized turbulent kinetic energy ($k/u_\tau{}^2$) for different turbulence models. The inertial centrifugal force causes high-velocity fluid particles to shift towards the outer side, leading to more pronounced turbulent fluctuations in that region. On the inner side, the swirl-switching of the secondary flow results in a concentrated turbulent kinetic energy shown as two vortices. Compared with the findings obtained from DNS, the LES model exhibits the closest agreement, followed by the SST k-ω model. The previous study found that the distribution of turbulent production terms in both the LES and SST k-ω models closely resembles the results obtained from DNS. The SST k-ω model, as a Reynolds-averaged method, encounters challenges in capturing the time-dependent swirl-switching phenomenon of the inner secondary flow, leading to lower values of turbulent kinetic energy on the inner side. Conversely, LES avoids this limitation and thus achieves the best predictive performance. However, the RST and Realizable k-ε models significantly overestimate the turbulence intensity in the inner region, resulting in higher values of predicted turbulent kinetic energy.

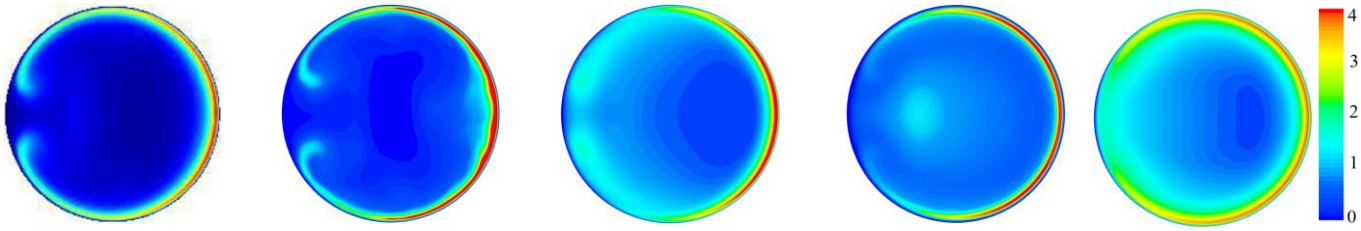

(**a**) DNS (**b**) LES (**c**) RST (**d**) SST *k*-*ω* (**e**) Realizable *k*-*ε*

Figure 4. Temporal fluctuation characteristics of different turbulence models: normalized turbulent kinetic energy.

Although LES has higher accuracy compared to other models, its computational cost increases rapidly, with a larger Reynolds number. Therefore, the RANS method to solve the Reynolds-averaged equation is an efficient and reasonable approach in engineering applications. Therein, the RST and Realizable *k*-*ε* models exhibit significant errors in simulating secondary flows in the plane. The SST *k*-*ω* model combines the advantages of the *k*-*ω* model in calculating low-Reynolds-number flows near the wall and the *k*-*ε* model in far-field calculations, which can be better used to study the flow field information in curved pipes. Considering the computational precision and efficiency of various turbulence models, the SST *k*-*ω* model was chosen for the subsequent study of the flow instability in the FMW.

In order to verify the accuracy of the SST *k*-*ω* model, the numerical results of the driving pump with different rotational speeds are compared with the PIV experimental data [19]. The experiment revealed that the flow field exhibited a non-uniform distribution of the streamwise velocity and spatial instability of the secondary flow in the cross-section. Here, the test case with 250 rpm is selected for the comparison validation, and the fluid velocity in the FMW is shown in Figure 5. The mean velocities along the main flow direction obtained using the flowmeter, PIV, and numerical simulation are 0.78, 0.79, and 0.85 m/s, respectively. The maximum error is less than 9%, which verifies the reliability of the numerical method.

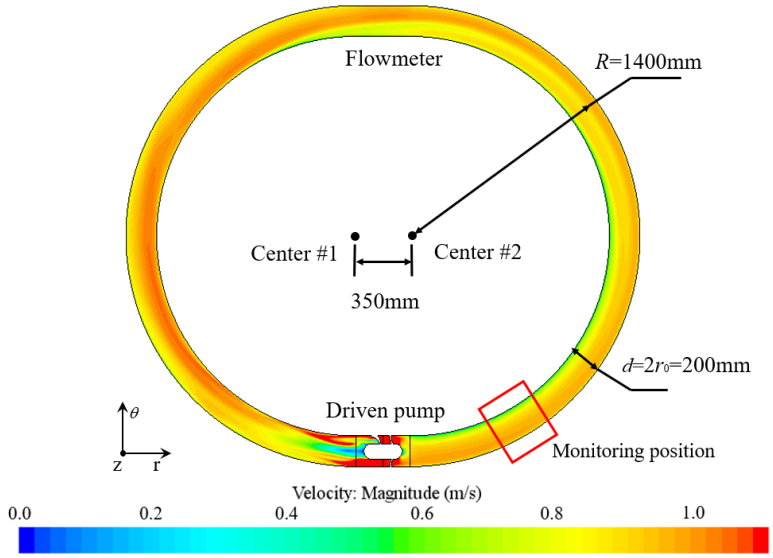

Figure 5. Fluid velocity and monitoring position of FMW.

The velocity distributions in the radial direction of the FMW can be obtained using PIV and numerical simulation methods, as shown in Figure 6. Therein, the *x*-axis is the non-dimensional ratio between the distance to the center and the radius, and the *y*-axis is the velocity value divided by the average velocity to obtain the dimensionless value of

the velocity. As can be seen from the figure, the velocity distribution measured via PIV is almost consistent with the numerical solution. The velocity gradually increases from the inner region to the outer region, indicating the presence of clear velocity stratification. However, it should be noted that the relatively big tracer particles in the boundary layer can result in data loss using the PIV method. The experiment revealed that the flow field exhibited a non-uniform distribution of the streamwise velocity and spatial instability of the secondary flow in the cross-section.

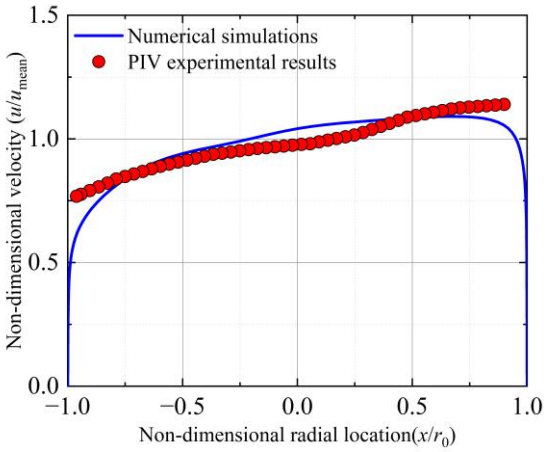

Figure 6. Comparison of non-dimensional velocity versus different methods.

3. Analysis of Flow Instability and Mechanical Energy Loss in FMW

3.1. Parameters to Quantitatively Evaluate Flow Instability

Although the FMW has some additional advantages compared to rigid-body gyrostabilizers, the effect of the spatiotemporal characteristics of the fluid field in the FMW requires further investigation. The instantaneous velocities of turbulent flow at any spatial point vary over time, and different spatial points exhibit different temporal fluctuation patterns, which means that the movement of fluid particles in a turbulent flow field is irregular both in time and space, as depicted in Figure 7. Thus, in classical turbulence theory, various physical quantities in a turbulent flow field are considered random variables that fluctuate in both time and space. Under the influence of different typical parameters of the FMW, the flow instability is mainly reflected in two aspects.

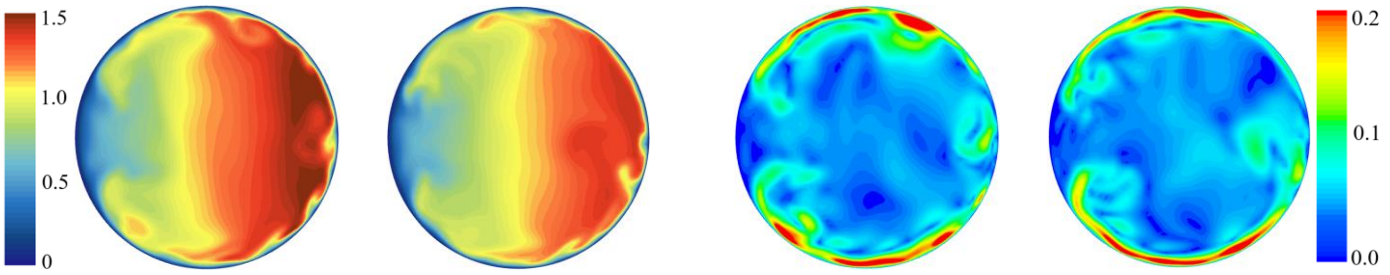

Figure 7. Temporal instability phenomenon: velocity fluctuations at different times. (**a**) Streamwise velocity (time 1); (**b**) streamwise velocity (time 2); (**c**) in-plane velocity (time 1); (**d**) in-plane velocity (time 2).

On the one hand, the temporal instability due to velocity fluctuation is represented by turbulent kinetic energy ($k = u_i'^2/2$). The higher the value of turbulent kinetic energy, the greater the magnitude of velocity fluctuations in the flow field over time. The radial distribution of scaled turbulent kinetic energy is compared in Figure 8, where the magnitudes are higher in the outer region of the high-velocity region. The distribution of turbulent

kinetic energy throughout the entire cross-section is influenced by the streamwise velocity distribution, exhibiting non-uniform characteristics. Therefore, the overall temporal instability can be determined by volume-integrating the turbulent kinetic energy in the flow field, as follows:

$$K_{all} = \iiint \frac{u_i'^2}{2} dV \tag{8}$$

where K_{all} represents the overall temporal instability, $u_i'^2/2$ denotes the turbulent kinetic energy, and the integral is the volume of the FMW.

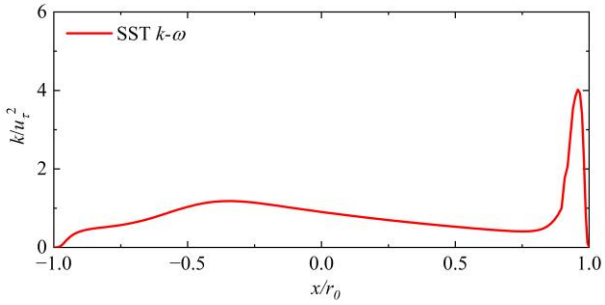

Figure 8. Radial distribution of turbulent kinetic energy.

On the other hand, spatial instability is evident in the radial stratification of streamwise velocity and the secondary flow in the plane, as indicated in Figure 9. The combination of streamwise velocity and in-plane secondary flow results in fluid particles displaying a spiral forward motion [41], which can significantly affect the stability of the FMW flow field, leading to variations in energy losses and instability in precession moments.

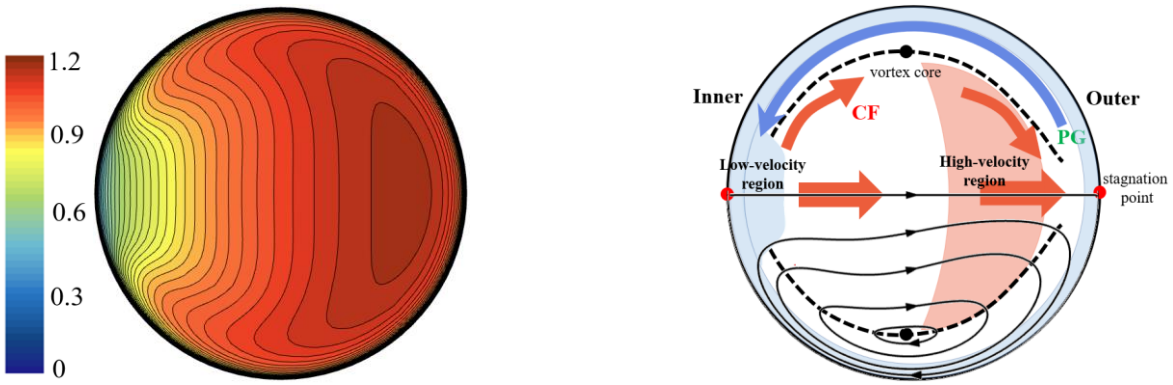

Figure 9. Spatial instability phenomenon. (**a**) Radial stratification of streamwise velocity; (**b**) secondary flow in the plane.

Compared to the rigid-body gyrostabilizer, the spatial instability of the flow field in the FMW can be attributed to two factors: the non-uniform distribution of the streamwise velocity and the convection effect of the in-plane secondary flow.

Firstly, the streamwise velocity is influenced by the centrifugal force in the curved pipe, resulting in a gradual increase in velocity from the inner to the outer region, as shown in Figure 9a. The presence of fluid viscosity further intensifies the non-uniform variation in velocity, with significant differences in the boundary layer velocity gradients between the inner and outer sides, as illustrated in Figure 10, which significantly impacts fluid resistance. Unlike the constant angular velocity during rigid rotation, the fluid velocity at the wall is zero, leading to a non-uniform angular velocity distribution. Therefore, in this study, the non-uniformity of the angular velocity was defined to analyze the streamwise instability. The angular velocity distribution along the centerline is obtained by dividing the

streamwise velocity of fluid particles by the distance from the center of the pipe ($\omega = u_\theta / x$). The variance ($S^2(\omega)$) of this angular velocity is then calculated as a measure of the non-uniformity of the cross-section, with a sampling interval of $0.02r_0$. Finally, the overall angular velocity instability of the flow field is quantified by multiplying the variance in angular velocity by the volume of the FMW, which is Equation (9).

$$S^2(\omega)_{all} = V \times S^2(\omega) \tag{9}$$

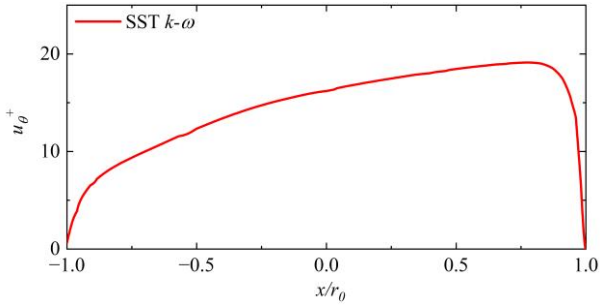

Figure 10. Radial distribution of streamwise velocity.

Next, in Figure 9b, under the combined influence of centrifugal force (CF) and the radial pressure gradient (PG) in the plane, the secondary motion significantly affects the flow field. The high-velocity fluid in the fully developed region experiences movement from the inner side to the outer side, primarily driven by centrifugal force, resulting in a high-velocity region on the outer side. Simultaneously, the low-velocity fluid near the wall moves inward along the wall under the influence of the pressure gradient, forming a low-velocity region on the inner side, as shown in Figure 9a. The intersection of these two motion patterns creates two stagnation points at the centerline positions on the inner and outer sides. Consequently, this study defined the swirl intensity of secondary flow as a measure of convection strength in the plane. By integrating the sum of the radial (u_r) and axial (u_z) velocity vectors in the flow field, the swirl intensity of secondary flow of the entire flow field ($I_{s\text{-}all}$) is obtained using Equation (10).

$$I_{s-all} = \iiint \sqrt{(u_r^2 + u_z^2)} dV \tag{10}$$

Moreover, numerical simulations were performed to acquire the distribution of streamlines of the secondary flow, and it was found that the higher the swirl intensity of secondary flow, the closer the vortex core is to the wall, as shown in the lower side of Figure 9b. Hence, a more comprehensive evaluation of the in-plane instability of the FMW can be achieved by evaluating the location of the vortex core of the secondary flow.

3.2. Flow Instability Versus Typical Parameters of FMWs

The fluid momentum wheel studied in this paper was a closed toroidal structure, and its typical parameters can be summarized as the pipe diameter (d), radius of curvature (R), and bulk velocity (u_b), as shown in Figure 1a. Variations in these parameters affect the spatiotemporal characteristics of the flow field in the FMW, resulting in corresponding changes in fluid resistance. This section used evaluation parameters to discuss the influence of typical parameters of FMWs on flow instability.

3.2.1. Pipe Diameter (d)

The pipe diameter plays a crucial role in determining the bending degree of the FMW, which affects the rate of velocity direction changes in space, as well as the magnitude of the centrifugal inertial force and the distribution of pressure gradients. Furthermore, the pipe diameter influences the pipe volume, which in turn affects the overall strength of instability

in the flow field. Table 2 provides the case parameters for analyzing the impact of the pipe diameter on the instability of the FMW.

Table 2. Flow field instability for different pipe diameters.

Case	d (m)	R (m)	u_b (m/s)	$S^2\ (\omega)_{all}$	$I_{s\text{-}all}$	K_{all}
1	0.1	1	1	0.01018	0.00121	0.00015
2	0.2	1	1	0.03505	0.00523	0.00044
3	0.3	1	1	0.07352	0.01118	0.00092

Through numerical calculations, it was found that increasing the pipe diameter while keeping other physical quantities constant reduces the stratification phenomenon in the cross-sectional streamwise velocity, which can be attributed to the greater centrifugal force. Under the squeezing effect of centrifugal force, the high-velocity region on the outer side extends towards both sides along the pipe wall, transforming its profile from a crescent shape to a C-shape, as shown in Figure 11. Consequently, the distribution of the streamwise velocity becomes more uniform, and the stratification phenomenon is weakened.

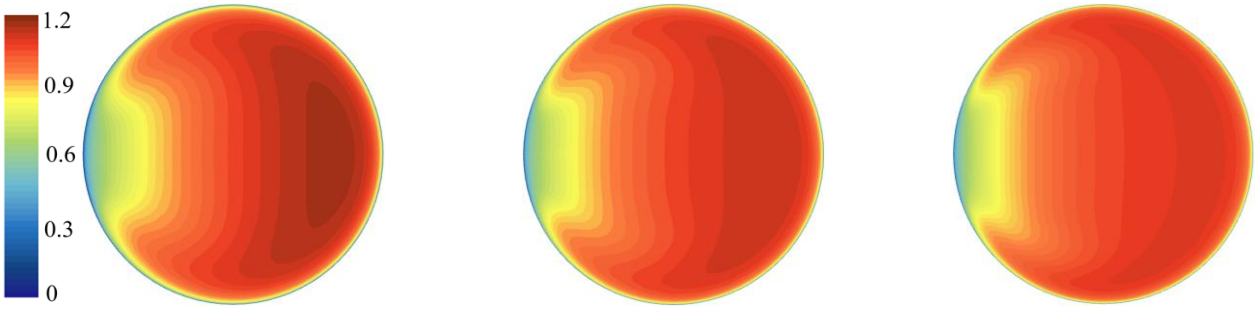

(**a**) d = 0.1 m (**b**) d = 0.2 m (**c**) d = 0.3 m

Figure 11. Stream wise velocity distributions in the cross-section for different pipe diameters.

Furthermore, in Figure 12, it can be seen that as the pipe diameter increases, the angular velocity of the inner region ($x/r_0 < 0$) increases, while the magnitude decreases and becomes smoother in the outer region ($x/r_0 > 0$). Consequently, there is a reduction in the non-uniformity of the in-plane angular velocity. Considering the instability of streamwise velocity in the overall flow field, the overall non-uniformity of the angular velocity becomes larger due to the increase in volume caused by the pipe diameter, and the results are summarized in Table 2.

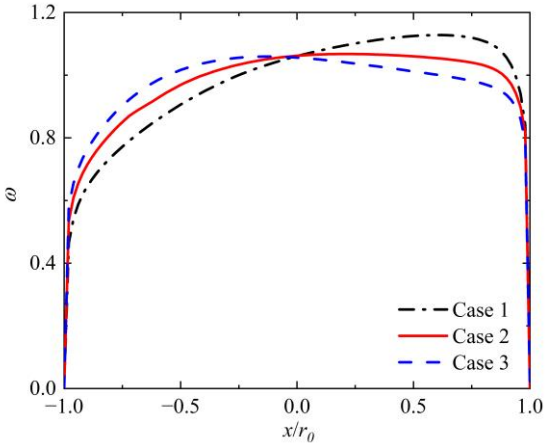

Figure 12. Angular velocity along the centerline for different diameters.

In the plane, an increase in the pipe diameter implies a relative increase in the curvature ratio, leading to an enhanced imbalance between the centrifugal force and the radial pressure gradient. Secondary flow is generated by the imbalance between the centrifugal force and the radial pressure gradient, and its scale and distribution are closely related to the mechanical properties. Based on the findings of this study, in the high-velocity region where turbulence is fully developed, the centrifugal force dominates and moves towards the outer region, while in the low-velocity region near both side walls, the pressure gradient dominates and shifts towards the inner region. The radial velocity (u_r) and axial velocity (u_z) in the plane increase, as shown in Figure 13. However, this also accompanies a notable reduction in the influence range of the secondary flow. From the streamline perspective, the vortex core of the secondary flow moves from the center towards the outer side and becomes closer to the pipe wall, which indicates that the convective action near the wall intensifies the exchange of fluid particles in the plane, enhancing the instability of the FMW. Furthermore, the inner streamlines displayed in Figure 13a approach the centerline horizontally and then gradually increase the inclination angle and shift towards both sides in Figure 13b,c. This also implies a reduced influence of the secondary flow on the region near the centerline, instead focusing more on the wall surfaces. The integration results in Table 2 confirm an overall increase in the swirl intensity of secondary flow, leading to enhanced instability in the plane.

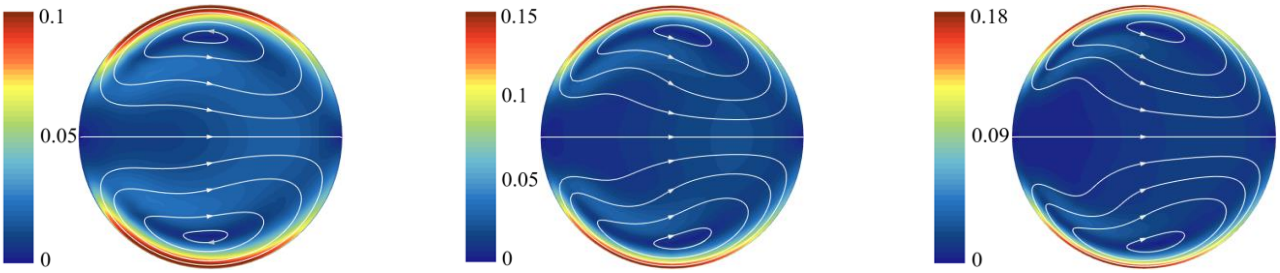

(**a**) d = 0.1 m (**b**) d = 0.2 m (**c**) d = 0.3 m

Figure 13. In-plane velocity magnitude overlaid with the streamline for different pipe diameters.

Turbulent kinetic energy represents the magnitude of fluctuations in instantaneous velocity concerning the time-averaged velocity and is an important parameter to measure the temporal instability characteristics of the FMW flow field. The velocity distribution is notably influenced by the centrifugal force, resulting in significant changes in the local Reynolds number, which is smaller on the inner side than on the outer side, and a corresponding change in the turbulent kinetic energy. Moreover, with an increase in the pipe diameter, the maximum value of cross-sectional turbulent kinetic energy decreases and becomes more concentrated near the wall in Figure 14. This phenomenon is also related to the transition of the velocity profile from a crescent shape to a C-shape, with a decrease in the velocity gradient on the outer side and a weakening of instability. However, the overall turbulent kinetic energy of the flow field gradually increases due to the expanded cross-sectional area resulting from the larger diameter of the FMW. This trend indicates a gradual enhancement of temporal instability in the overall flow field of the momentum wheel, as presented in Table 2.

3.2.2. Radius of Curvature (R)

The velocity direction of fluid particles changes more rapidly as the radius of curvature decreases, which results in a stronger centrifugal force and pressure gradient imbalance acting on the fluid and a more pronounced secondary motion in the plane. As a result, the instability of the flow field undergoes significant changes. Next, the effect of the radius of curvature was analyzed, and Table 3 provides relevant parameter information for the cases.

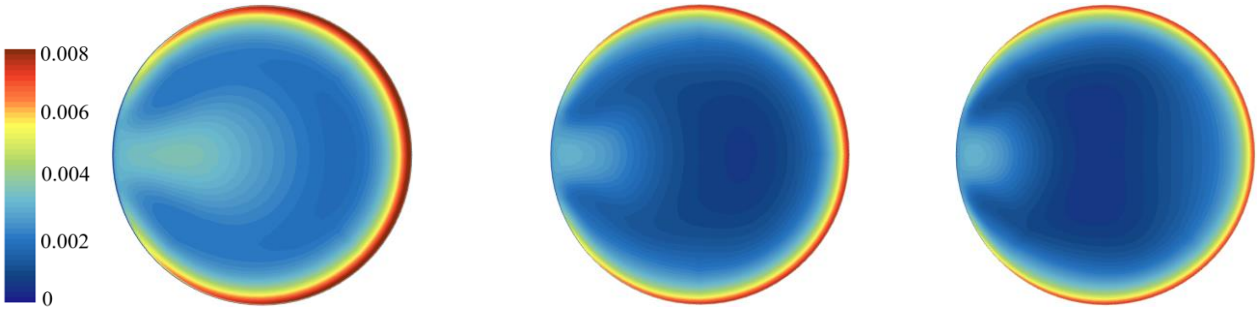

(**a**) d = 0.1 m (**b**) d = 0.2 m (**c**) d = 0.3 m

Figure 14. Turbulent kinetic energy for different pipe diameters.

Table 3. Flow field instability for different radii of curvature.

Case	d (m)	R (m)	u_b (m/s)	S^2 $(\omega)_{all}$	$I_{s\text{-}all}$	K_{all}
4	0.1	0.5	1	0.00924	0.00070	0.00006
5	0.1	1	1	0.01018	0.00121	0.00015
6	0.1	2	1	0.01027	0.00213	0.00035

The increase in the curvature radius causes a corresponding decrease in the curvature ratio of the FMW and a reduction in the centrifugal inertial effect on the fluid, which leads to a slowdown in the phenomenon of velocity stratification, as depicted in Figure 15. On the inner side, the low-velocity region gradually converges towards the centerline from both sides with a decreased impact range, while the impact range of the high-velocity region decreases but its magnitude increases on the outer side. By comparing Figure 15a,c, the larger centrifugal force compresses the high-velocity particles, causing them to expand towards both sides and create a protrusion towards the inner side.

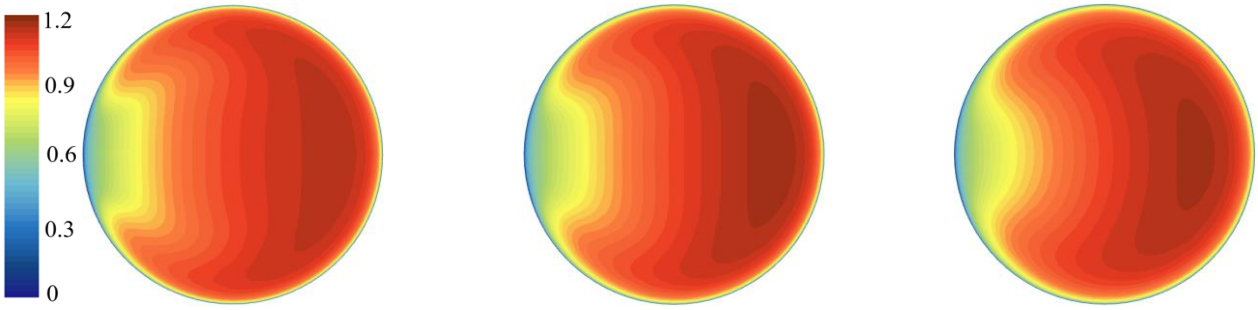

(**a**) R = 0.5 m (**b**) R = 1 m (**c**) R = 2 m

Figure 15. Streamwise velocity distributions in the cross-section for different radii of curvature.

Furthermore, in the angular velocity distribution along the centerline depicted in Figure 16, Case 4 and 6 data have been subjected to scaling. Case 4 exhibits a relatively higher uniform angular velocity distribution than the others, owing to the inward displacement of high-velocity particles caused by the compressing centrifugal force. In contrast, the distributions in Cases 5 and 6 exhibit significant similarities with a larger difference between their inner and outer regions. Considering the influence of scaling parameters, the actual instability of angular velocity along the centerline decreases as the radius of curvature increases. However, in terms of the overall flow field of the FMW, increasing the radius of curvature leads to a larger volume of the flow field, thereby amplifying the overall instability of angular velocity and enhancing the spatial instability of the streamwise direction, as shown in Table 3.

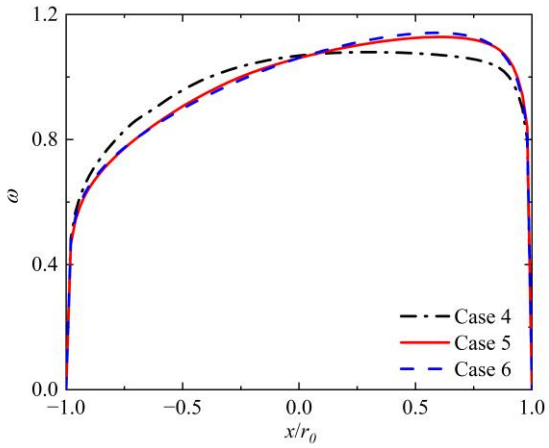

Figure 16. Angular velocity distribution along the centerline for different radii of curvature: Case 4 with a scaling factor of 0.5 and Case 6 with a scaling factor of 2.

Table 3 shows that with the increase in the curvature radius, the swirl intensity of secondary flow increases, and the spatial instability in the plane also becomes enhanced. Due to the increase in the curvature radius while keeping the diameter constant, the curvature ratio of the FMW decreases, weakening the centrifugal inertial of the fluid and reducing the secondary flow. As a result, the magnitude of the in-plane velocity decreases in Figure 17. However, in the streamline diagram of the secondary flow, the vortices gradually move away from the pipe wall and shift towards the inner side and center of the pipe. The inner streamlines, which are initially inclined in Figure 17a, become more horizontal in Figure 17b,c, indicating an enlargement of the range of influence of the secondary flow. On the other hand, an increase in the radius of curvature leads to an expansion of the flow field volume. Therefore, when integrating the swirl intensity of secondary flow over this volume, the overall swirl intensity of secondary flow in the FMW becomes strengthened.

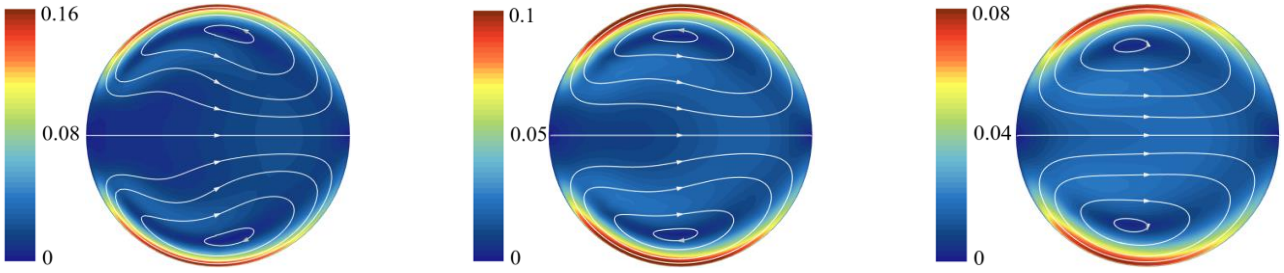

(**a**) R = 0.5 m (**b**) R = 1 m (**c**) R = 2 m

Figure 17. In-plane velocity magnitude overlaid with the streamline for different radii of curvature.

Regarding the temporal instability of the flow field, Figure 18 demonstrates that the pipe diameter and velocity remain constant across different cases, ensuring a consistent Reynolds number and resulting in minimal variations in the magnitude range of turbulent kinetic energy. However, as the influence range of the secondary flow expands, turbulent kinetic energy increases in the fully developed turbulent region located further away from the wall. Moreover, the fluid volume increases as the radius of curvature increases, thus gradually increasing the overall turbulent kinetic energy of the flow field, which indicates that the temporal instability of the flow field of the FMW gradually strengthens, as shown in Table 3.

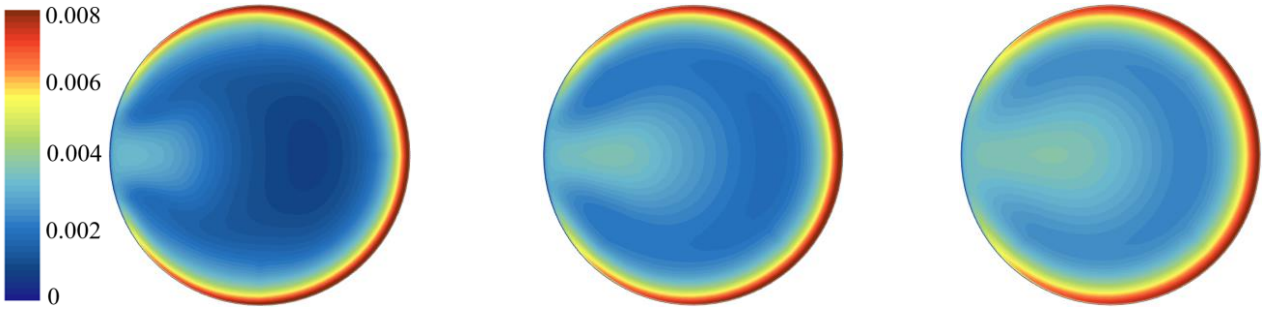

(**a**) R = 0.5 m (**b**) R = 1 m (**c**) R = 2 m

Figure 18. Turbulent kinetic energy distributions for different radii of curvature.

3.2.3. Velocity (u_b)

The increase in velocity enhances the inertial force of the fluid, resulting in more pronounced fluctuations and variations in turbulent eddies. Larger-scale eddies are more susceptible to stretching and fragmenting into smaller-scale eddies, which convert mechanical energy into thermal energy due to the fluid viscosity. Meanwhile, velocity also affects the balance between the centrifugal force and pressure gradient, and spatial instability in the flow field changes with it. Table 4 below provides the parameter information for the cases.

Table 4. Flow field instability for different velocities.

Case	d (m)	R (m)	u_b (m/s)	S^2 $(\omega)_{all}$	$I_{s\text{-}all}$	K_{all}
7	0.1	1	1	0.01018	0.00121	0.00015
8	0.1	1	2	0.01943	0.00228	0.00054
9	0.1	1	5	0.04626	0.00534	0.00275

Figure 19 presents the scaled streamwise velocity distributions for various velocities. Due to the consistent curvature of the momentum wheel structure, the rate of particles changing their velocity direction is similar, resulting in a similar stratification phenomenon. However, as the velocity increases, the inertial effect of the fluid is enhanced, causing the balance between the inertial force and the viscous force to shift closer to the wall, and the boundary layer becomes thinner. Moreover, there is a slight decrease in both the scaled velocity magnitude and the impact range of the high-velocity region on the outer side.

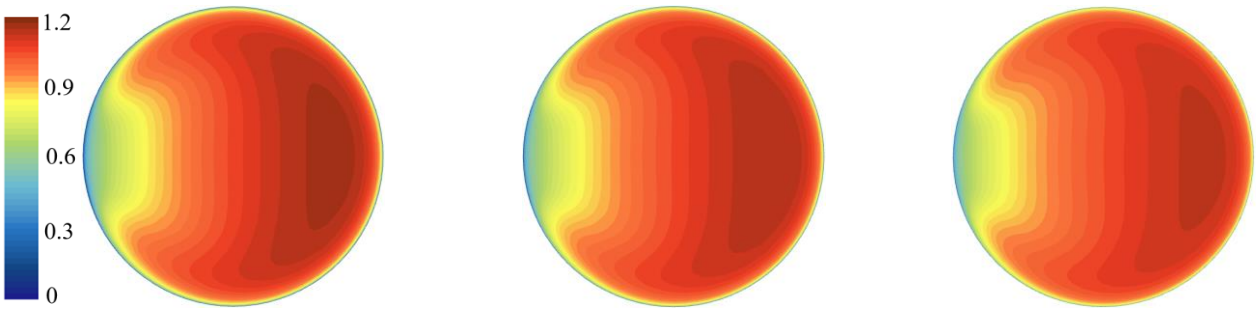

(**a**) u_b=1 m/s (**b**) u_b=2 m/s (**c**) u_b=5 m/s

Figure 19. Streamwise velocity distributions in the cross-section for different velocities: Case 8 with a scaling factor of 0.5 and Case 9 with a scaling factor of 0.2.

In Figure 20, the data of Cases 8 and 9 are scaled, revealing minimal differences in the distribution of angular velocities along the centerline in different cases. Specifically, Case 9 exhibits a more uniform angular velocity distribution than the other cases. However,

by considering the influence of scaling factors, the actual instability of angular velocity becomes larger with an increasing velocity. Therefore, even though the geometric models are consistent across different cases, the streamwise direction instability of the flow field becomes more significant with an increasing velocity, as indicated in Table 4.

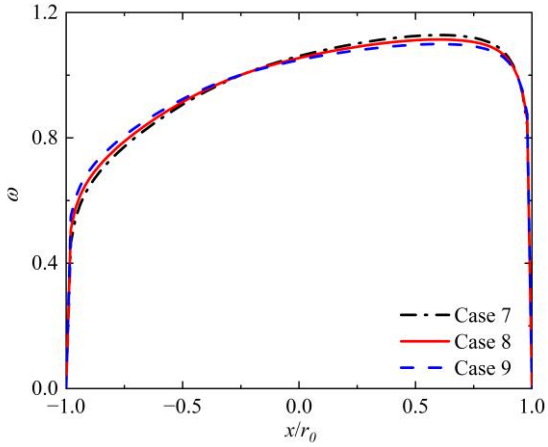

Figure 20. Angular velocity along the centerline for different velocities: Case 8 with a scaling factor of 0.5 and Case 9 with a scaling factor of 0.2.

The increase in velocity enhances the in-plane convection effect, resulting in a higher radial velocity (u_r) and axial velocity (u_z) in the plane. However, after numerical scaling in Figure 21, the in-plane velocity magnitude and streamline distribution remain almost unchanged, implying that the distribution of secondary flow streamlines is closely associated with the curvature ratio. The velocity variation affects the strength of centrifugal forces and the radial pressure gradient, but the imbalance between the two forces is not fundamentally altered. Therefore, the magnitude of in-plane velocity and instability increases with a higher bulk velocity, but the distribution of streamline patterns is primarily determined by the velocity vector, rather than its magnitude, thus not exhibiting significant variations.

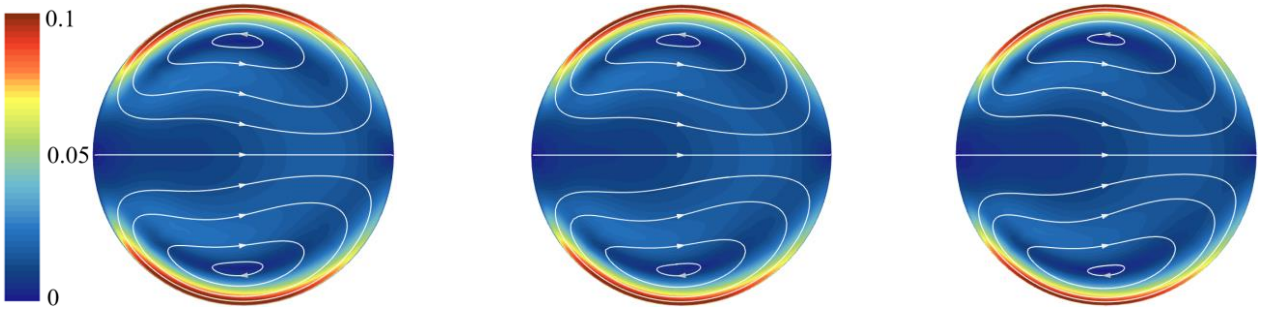

(**a**) u_b=1 m/s (**b**) u_b=2 m/s (**c**) u_b=5 m/s

Figure 21. In-plane velocity magnitude overlaid with the streamline for different velocities: Case 8 with a scaling factor of 0.5 and Case 9 with a scaling factor of 0.2.

As the velocity increases, fluctuation and disorder in the flow field significantly intensify, and the turbulent kinetic energy of the cross-section is increased. While other geometric parameters remain constant, the overall turbulent kinetic energy of the entire flow field gradually increases, indicating the growing temporal instability of the flow field, as shown in Table 4. Notably, Figure 22 demonstrates that the scaled turbulent kinetic energy decreases as the velocity increases, suggesting a non-constant relationship between the two. This observed phenomenon may be attributed to the influence of viscosity, which imposes limitations on the development of turbulent kinetic energy.

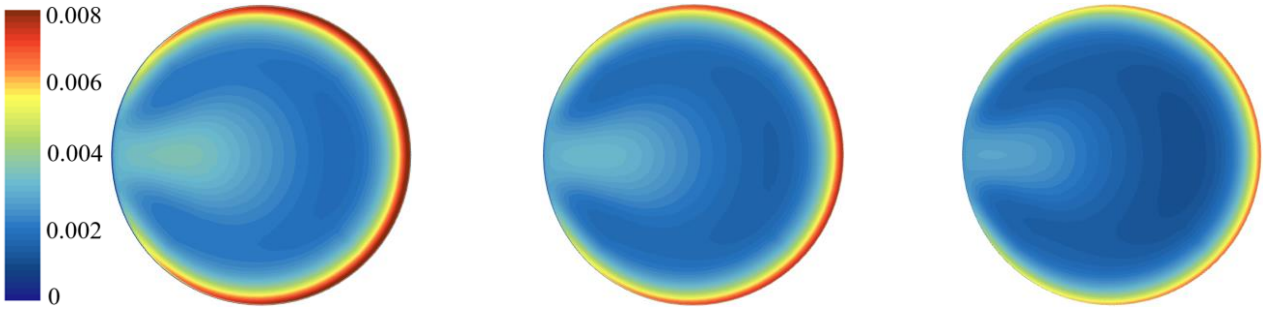

(**a**) u_b=1 m/s (**b**) u_b=2 m/s (**c**) u_b=5 m/s

Figure 22. Turbulent kinetic energy for different velocities: Case 8 with a scaling factor of 0.25 and Case 9 with a scaling factor of 0.04.

3.2.4. Influence of Dimensionless Factors on the Flow Instability

The sensitivity of the instability in the flow field of the FMW varies depending on typical parameters. The velocity affects the magnitude of the inertial force, while the pipe diameter and radius of curvature influence the balance between centrifugal force and the radial pressure gradient, leading to changes in flow field stability. Increasing the geometric (d and R) and fluid (u_b) parameters of the FMW also increases the measurement parameters of flow field instability. In terms of the impact of different parameters on the flow field instability, bulk velocity has the greatest influence on instability, followed by the pipe diameter and curvature radius. Furthermore, dimensionless parameters, such as the Reynolds number ($Re = \rho u_b d/\nu$) and curvature ratio ($\kappa = r_0/R$), can be used to evaluate the instability of the FMW based on their interrelationships. Among these parameters, the Reynolds number represents the ratio of inertial forces to viscous forces and plays a crucial role in determining the turbulent state of a flow field. On the other hand, the curvature ratio is a geometric parameter that describes the rate that fluid particles change their velocity. The curvature ratio directly affects the strength of the inertial centrifugal force and significantly impacts velocity redistribution. It is also necessary to perform dimensionless processing of the measurement parameters of instability to eliminate the influence of parameter changes on the results and obtain more generalized and reliable conclusions.

For the spatial instability of the flow field, the non-uniformity of the angular velocity and the swirl intensity of secondary flow are processed as dimensionless. First, the angular velocity along the centerline is normalized by its average value ($\omega_0 = \omega/\overline{\omega}$), for which variance denotes the dimensionless non-uniformity of the angular velocity in the flow field, denoted as S^2 (w_0). In addition, the sum of the radial and axial velocity vectors is calculated and integrated across the entire flow field, which is normalized by the bulk velocity to obtain the dimensionless swirl intensity of secondary flow, as expressed in Equation (11).

$$I_s = \iiint \sqrt{(u_r^2 + u_z^2)} dV / \iiint u_b dV \tag{11}$$

Subsequently, the turbulent kinetic energy is integrated over the entire flow field, normalized by the integral of the velocity squared to quantify the temporal instability of the flow field in Equation (12).

$$K = \iiint \frac{u'^2_i}{2} dV / \iiint {u_b}^2 dV \tag{12}$$

In order to validate the feasibility of the dimensionless factors, Cases 10 and 11 in Table 5 are designed to ensure that under different conditions of the pipe diameter, radius of curvature, and velocity, the Reynolds number and curvature ratio remain consistent, thus excluding potential influences from other factors.

Table 5. Flow instability for the same dimensionless parameters.

Case	d (m)	R (m)	u_b (m/s)	Re	κ	S^2 (w_0)	I_s	K
10	0.1	1	2	2.25×10^5	0.05	0.20421	9.52×10^{-4}	0.00275
11	0.2	2	1	2.25×10^5	0.05	0.19691	9.83×10^{-4}	0.00270
Error	/	/	/	/	/	3.58%	−3.26%	2.03%

The same Reynolds number and curvature ratio suggest that the fluid particles experience similar centrifugal force, and the phenomenon of velocity stratification is fairly consistent in Figure 23a. Furthermore, Figure 24 displays the normalized angular velocity along the centerline for Cases 10 and 11, and their distributions essentially overlap, which suggests an approximate non-uniformity in the streamwise direction. The similarity in in-plane velocity and streamline distribution in Figure 23b suggests that the imbalance between the centrifugal force and pressure gradient has not substantially changed, and the in-plane instability remains similar. Finally, the distribution and magnitude of turbulent kinetic energy shown in Figure 23c are also highly similar. When considering the same Reynolds number and curvature ratio, the local Reynolds numbers in the flow field also remain consistent, according to Figure 23a,b. These findings provide evidence for the approximation of the spatiotemporal instability in the flow field with the same dimensionless parameters.

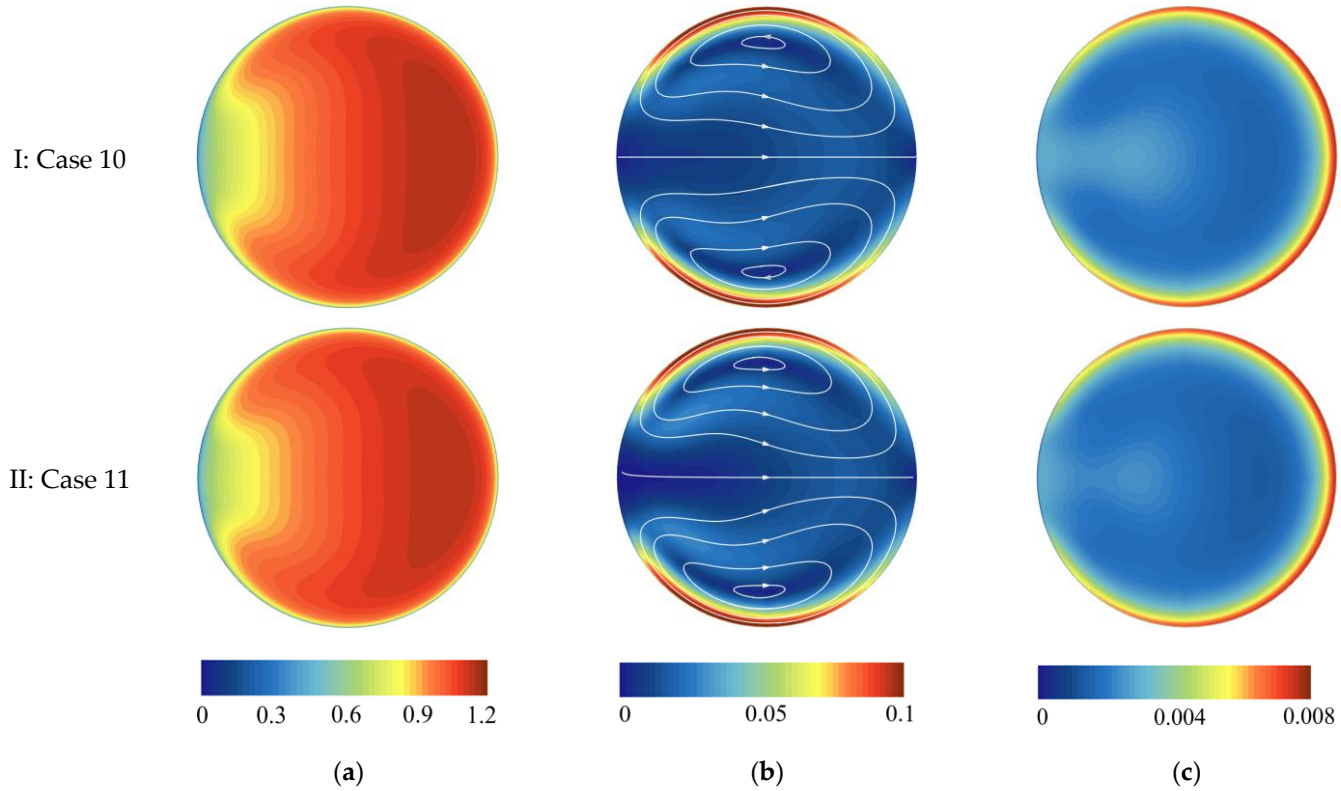

Figure 23. Spatiotemporal instability for same dimensionless parameters. (**a**) Streamwise velocity normalized by u_b; (**b**) in-plane velocity normalized by u_b; (**c**) turbulent kinetic energy normalized by ${u_b}^2$.

Table 5 summarizes the dimensionless instability results obtained from the flow field. The errors in the dimensionless instability are 3.58%, −3.26%, and 2.03%, respectively, indicating that using dimensionless parameters, such as the Reynolds number and curvature ratio, instead of conventional parameters, is a reasonable approach for investigating flow field instability.

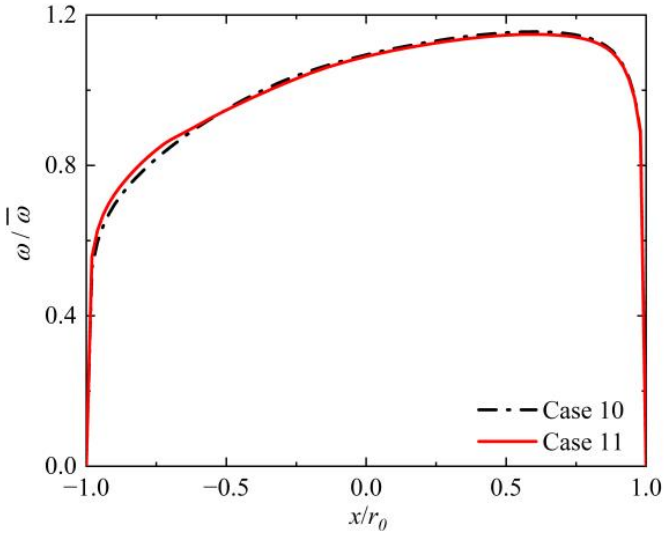

Figure 24. Normalized angular velocity distribution along the centerline for the same dimensionless parameters.

3.3. Influence of Flow Instability on Mechanical Energy Loss

In fluid dynamics, the increasing flow instability leads to heightened disorder and fluctuations in the turbulent flow. Fluid particles continuously collide under the vortices, which converts the kinetic energy into thermal energy dissipation and an associated increase in energy loss. This section aimed to analyze the relationship between flow field instability and energy loss.

Firstly, an analysis is conducted on the variation in fluid resistance under typical parameter influences. This study used the magnitude of wall shear stress to represent the changes in energy loss in the flow field. Due to the convective effect of secondary flow, the low-velocity fluid is shifted inward along the wall, while the high-velocity fluid moves outward. As a result, a low wall shear stress depression is formed in the inner region ($160° < \varphi < 200°$) in Figure 25. Conversely, in the outer region, where the velocity is relatively high, and distribution is relatively uniform, the wall shear stress exhibits a similar pattern to that of the velocity ($300° < \varphi < 60°$).

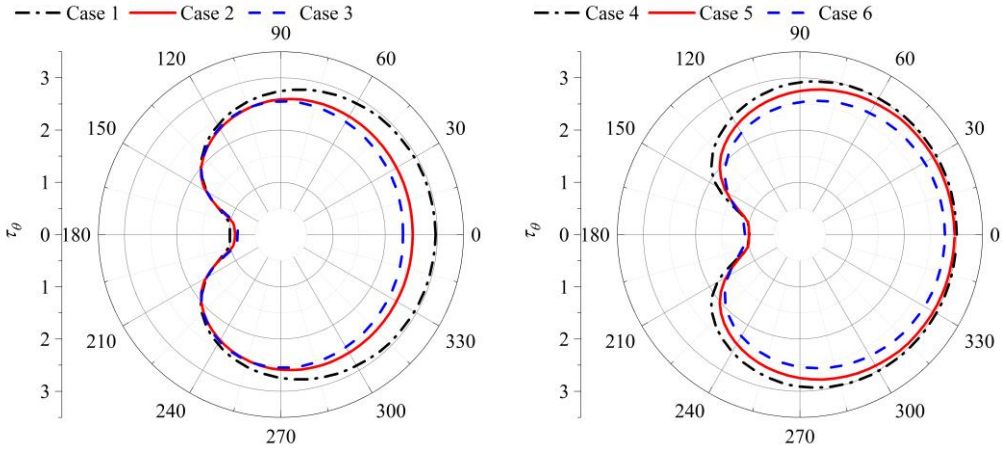

(**a**) (**b**)

Figure 25. *Cont.*

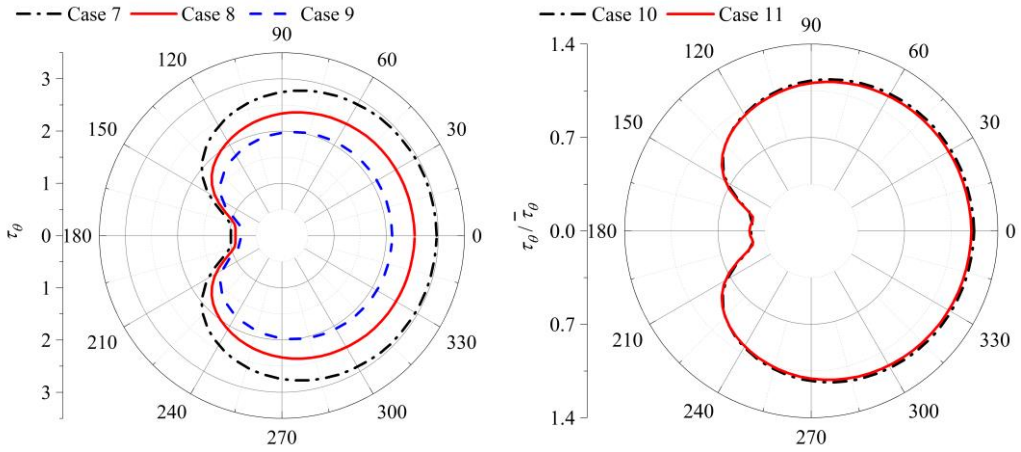

Figure 25. Wall shear force distribution. (**a**) Pipe diameter; (**b**) radius of curvature; (**c**) velocity: Case 8 with a scaling factor of 0.25 and Case 9 with a scaling factor of 0.04; (**d**) dimensionless parameters: normalized by the average value.

As the pipe diameter increases, the streamwise velocity distribution gradually transitions from a crescent shape to a C-shape due to the strong centrifugal force that squeezes high-velocity fluid toward the inner side. In Figure 25a, the velocity gradient decreases in the outer region, leading to an overall decrease in wall shear stress, with the largest difference occurring at $\varphi = 0°$. Furthermore, velocity distributions mainly maintain the crescent shape with the changes in the radius of curvature, and the distribution of wall shear stress is similar for each case, as shown in Figure 25b. As the radius of curvature increases, the centrifugal effect weakens, reducing the range of the high-velocity region and subsequently decreasing the magnitude of wall shear stress. However, in Case 4, the wall shear stress values are significantly higher near the vertical line region ($\varphi = 90°$) due to the obvious squeezing effect of centrifugal force. For cases with different velocities, the distributions of scaled wall shear stress in Figure 25c are similar due to the consistent stratification phenomenon of the streamwise velocity. The magnitude of scaled wall shear stress decreases nearly proportionally with the increasing velocity, indicating that the proportional coefficient between cases is slightly lower than the square of velocity changes. This is closely related to the mutual constraint between inertial forces and viscous forces in the boundary layer. Additionally, under the same conditions of the curvature ratio and Reynolds number, the near-wall characteristics of the flow field are similar, and the flow field exhibits similar instability. In Figure 25d, the curve distribution of normalized wall shear stress largely overlaps, suggesting similar distribution characteristics of fluid resistance.

The resistance is quantified by integrating the streamwise shear force on the pipe wall to investigate the impact of flow field instability on energy loss under typical parameter variations, as depicted in Equation (13).

$$\tau_{\theta-all} = \iint \tau_\theta dS \tag{13}$$

In the previous analysis, it was observed that as the diameter and radius of curvature increase, the magnitude of the wall shear force in the cross-section gradually decreases, as shown in Figure 25. However, the increase in the wall surface area results in an overall increase in the integral results, which is the increase in the resistance of the entire flow field, as demonstrated in Table 6. Conversely, variations in velocity have no effect on the geometric parameters of the FMW but significantly increase the magnitude of the wall shear force in the cross-section. Therefore, combining the previous data on flow field

instability (Tables 2–4), it can be seen that the resistance of the flow field increases with the enhancement of flow field instability.

Table 6. Area integral of wall shear force.

Case	$\tau_{\theta\text{-}all}$	Case	$\tau_{\theta\text{-}all}$	Case	$\tau_{\theta\text{-}all}$
1	2.39	4	1.28	7	2.39
2	4.37	5	2.39	8	8.32
3	6.34	6	4.53	9	43.97

Next, in order to further analyze the relationship between flow field instability and energy loss, some test cases are designed with various curvature ratios (0.01, 0.025, 0.05, 0.1, and 0.2) and different Reynolds numbers (1.13×10^5, 2.25×10^5, 5.63×10^5, 1.13×10^6, and 2.25×10^6).

For the spatial instability of the flow field, the in-plane secondary flow overlays the main flow in a curved pipe, thereby affecting the distribution of the streamwise velocity. From the previous results, it was found that an increase in the Reynolds number indicates an enhancement of inertial forces and an amplification of streamwise velocity non-uniformity. However, the normalized non-uniformity of angular velocity in the flow field decreases with an increase in the Reynolds number, as shown by the scatter plot of different colors in Figure 26a. The decrease in boundary layer thickness prevents low-velocity particles from escaping the viscous constraints, impeding their transport to the inner regions based on the secondary flow along the pipe wall. Consequently, the relative difference in velocities between the inner and outer regions decreases, resulting in a decline in angular velocity non-uniformity. On the other hand, an increase in the curvature ratio shows an enhancement of the secondary motion, which significantly affects the distribution of the streamwise velocity and changes the local Reynolds number of the flow field. Initially, the secondary flow leads to an increase in the non-uniformity of the angular velocity. As the curvature ratio increases, the centrifugal force strengthens, and the squeezing velocity moves towards both sides, transforming the profile of the high-velocity region into a crescent shape and C-shape. This phenomenon reduces the difference between the inner and outer velocities and decreases the non-uniformity of the angular velocity.

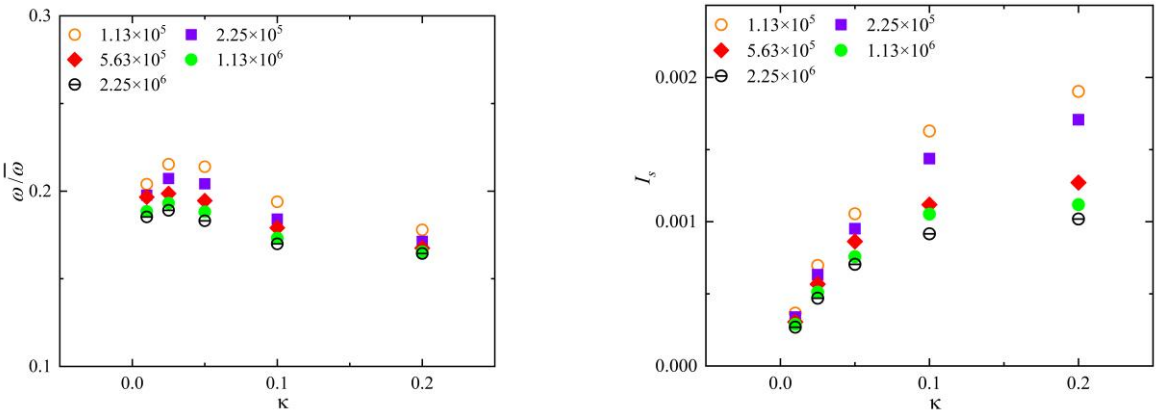

(**a**) Angular velocity non-uniformity (**b**) Swirl intensity of the secondary flow

Figure 26. Spatial instability for different dimensionless parameters.

As the curvature ratio increases, the radial imbalance effect significantly enhances the secondary flow intensity, as depicted by the x-axis variation in Figure 26b. Along with the increase in Reynolds number, the velocity gradient of the boundary layer amplifies, leading to a decrease in the distribution range for the low-velocity fluid. Consequently, the secondary flow becomes more concentrated near the wall, causing a decrease in its impact range and subsequently weakening the swirl intensity of the secondary flow. At

low curvature ratios, the influence of the curvature ratio outweighs that of the Reynolds number. However, as the curvature ratio increases, the influence of the Reynolds number gradually becomes dominant based on the parameter I_s.

For the temporal instability of the flow field, the fluctuation of the flow field strengthens when the Reynolds number increases, as shown in Figure 22. However, a decrease in the fluid boundary layer and viscous constraints make the transition from laminar to turbulent flow more challenging, which results in a gradual decrease in the normalized turbulent kinetic energy. The convective effect of the secondary flow induced by the curvature ratio affects the streamwise velocity distribution and the relative strengths of local inertial and viscous forces, significantly impacting the turbulent kinetic energy. Specifically, the velocity distribution transforms from circular to elliptical, crescent, and C-shape, showing the radial stratification with a low-speed region on the inner side and a high-speed region on the outer side. Similarly, the distribution of turbulent kinetic energy demonstrates a similar pattern, with higher values near the outer wall. After dimensionless treatment of the temporal instability, it is observed that for the curvature ratio $\kappa < 0.1$ in Figure 27a, the turbulent kinetic energy decreases as the curvature ratio increases, indicating that the non-uniform distribution of streamwise velocity reduces the temporal fluctuation of the flow field. However, at a curvature ratio of $\kappa = 0.2$, the strong squeezing effect of the centrifugal force causes the high-velocity fluid to extend from the center towards the side walls, which leads to a more uniform distribution of streamwise velocity, thus increasing the turbulent kinetic energy in the flow field.

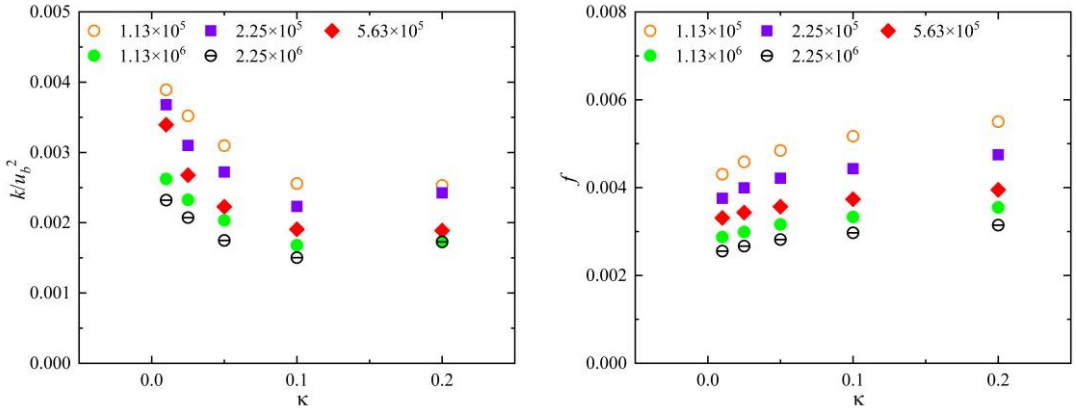

(**a**) Normalized turbulent kinetic energy (**b**) Fanning friction factor

Figure 27. Normalized turbulent kinetic energy and fanning friction factor with various curvature ratios.

The analysis of mechanical energy loss in the pipe flow commonly involves dimensionless friction factors, such as the Darcy friction factor (f) and the Fanning friction factor ($\lambda = 4f$). In this study, the Fanning friction factor was employed to evaluate the energy-loss characteristics of the flow field. An increase in the Reynolds number implies a decrease in the boundary layer thickness and an increase in the velocity gradient. Despite a significant increase in the magnitude of the wall shear stress, there is a relative decrease in both the dimensionless instability of the flow field and the Fanning friction factor, as shown in Figure 27b. On the other hand, the secondary flow enhances the instability and energy loss by changing the velocity distribution with the increase in the curvature ratio, and the friction factor slightly increases. Furthermore, the influence of the curvature ratio on the friction factor is gradually reduced as the curvature ratio increases, which is consistent with the trend observed in I_s, as shown in Figure 26b. Considering the relative impact of these two dimensionless parameters, the Reynolds number has a greater influence on the Fanning friction factor than the curvature ratio.

4. Conclusions

The inertial centrifugal force and radial pressure gradient induce the in-plane secondary flow and non-uniform velocity distribution, significantly affecting the fluid resistance. Additionally, the temporal instability caused by turbulent fluctuation also affects the energy conversion of the flow field. Based on previous research on the energy loss mechanism in the FMW, this study used numerical simulation methods to analyze the effects of typical parameters on the flow field instability and mechanical energy loss. Some meaningful conclusions can be made as follows:

(1) This study conducted calculations using different turbulence models (LES, RST, SST k-ω, and Realizable k-ε models) and compared the results with DNS and experimental results. The differences in the streamwise and in-plane velocities and turbulent kinetic energy were further analyzed. Among the models, LES showed the best agreement in terms of spatial and temporal characteristics with high computational costs. However, the RST and Realizable k-ε models exhibited larger errors in the distributions of secondary flow and turbulent kinetic energy. The SST k-ω model provided high accuracy in both the Fanning friction factor and flow field characteristics while maintaining computational efficiency, and reproduced the velocity stratification phenomenon observed in experiments well. Therefore, the SST k-ω model was selected to analyze the influence of flow field instability on mechanical energy loss in the FMW.

(2) The flow characteristics of the FMW differ significantly from the rigid-body gyrostabilizer with a constant angular velocity due to the influence of fluid viscosity. Specifically, the flow field exhibits significant turbulent fluctuations with time and velocity stratification and in-plane secondary flow in the spatial characteristics. In the analysis of the spatiotemporal instability of the FMW flow field, the spatial instability parameters (angular velocity non-uniformity and swirl intensity of secondary flow) and temporal instability parameter (turbulent kinetic energy) were defined to assess the impact of typical design parameters on the flow field instability. The computational results demonstrated that the instability increases as the typical parameters (pipe diameter, radius of curvature, and velocity) increase. The in-plane secondary flow significantly affects the streamwise velocity distribution, transforming the profile of the high-velocity region on the outer side into a crescent shape and C-shape. Consequently, the angular velocity non-uniformity and the magnitude and distribution of turbulent kinetic energy change with it, ultimately influencing fluid resistance. Subsequently, the typical parameters were represented as dimensionless parameters (Reynolds number and curvature ratio). Under the same conditions of these dimensionless parameters, the flow field instability maintains good agreement, indicating that using dimensionless parameters to evaluate the flow field instability is reasonable enough.

(3) Finally, this study examined the impact of flow field instability on mechanical energy loss. The distribution of wall shear forces is closely related to the velocity distribution, showing a notable non-uniform distribution with higher values on the outer side compared to the inner side. The increase in typical parameters enhances the instability of the flow field, which leads to higher wall shear forces and increased resistance effects. Moreover, the flow field instability parameters are normalized, and the Fanning friction factor is employed to evaluate the energy loss characteristics of the flow field. Non-dimensional parameters are established to quantitatively evaluate the relationship between flow field instability and energy loss. The findings revealed that an increase in the Reynolds number corresponds to a decrease in the flow field instability and friction factor. Conversely, a rise in the curvature ratio amplifies the in-plane secondary motion of the flow field, resulting in an increased friction factor. When comparing their relative influences, it is evident that the Reynolds number has a significantly larger impact on the Fanning friction factor than the curvature ratio. Specifically, the curvature ratio has a stronger influence on the in-plane motion of the flow field, indirectly affecting the local Reynolds number and leading to changes in the friction factor.

This study analyzed the temporal fluctuation represented by turbulent kinetic energy to provide support for quantitatively evaluating the mechanical energy loss in the FMW. However, the RANS method employed in this study has limitations in capturing the details of temporal fluctuation characteristics in the flow field, such as the swirl-switching phenomenon of secondary flow in the main flow region. In the boundary layer near the wall, the stretching, deformation, and splitting of turbulent vortices affect the energy transfer and transformation. In future studies, LES or DNS methods will be used to investigate the near-wall turbulent structures and the relationship between the switching frequency of the secondary flow and the fluctuations in the wall shear force.

Author Contributions: Conceptualization, W.W.; methodology, K.Z. and H.L.; software, Y.L. and Y.D.; validation, Y.L. and K.Z.; formal analysis, L.W. and H.L.; investigation, K.Z. and Y.D.; resources, L.W. and H.L.; data curation, W.W., Y.L. and K.Z.; writing—original draft preparation, K.Z.; writing—review and editing, W.W., L.W., H.L. and Y. H.; visualization, Y.L. and H.L.; supervision, L.W., H.L. and Y.H.; project administration, Y.D., H.L. and W.W.; funding acquisition, Y.D., Y.H. and W.W. All authors have read and agreed to the published version of the manuscript.

Funding: The authors are grateful to all organizations that funded the research in this paper, which was financially supported by the National Natural Science Foundation of China (General Program) (Grant No. 52271259), the National Natural Science Foundation of China (Grant No. 51679034), and the Dalian Innovation Team Support Plan in key areas (2019RT12).

Institutional Review Board Statement: Not applicable.

Informed Consent Statement: Not applicable.

Data Availability Statement: Data are contained within the article.

Acknowledgments: The authors are grateful to all organizations that funded the research in this paper, which was financially supported by the National Natural Science Foundation of China (General Program) (Grant No. 52271259), the National Natural Science Foundation of China (Grant No. 51679034), and the Dalian Innovation Team Support Plan in key areas (2019RT12).

Conflicts of Interest: The authors declare no conflict of interest.

References

1. Wang, Y.; Wang, H.; Zhou, B.; Fu, H. Multi-dimensional prediction method based on Bi-LSTMC for ship roll. *Ocean Eng.* **2021**, *242*, 110106. [CrossRef]
2. Kim, G.-H.; Hwang, S.; Lee, S.-H.; Lee, J.-H.; Hwangbo, J.; Kim, K.-S.; Paik, K.-J. A Numerical Study on the Performance of the 66k DWT Bulk Carrier in Regular and Irregular Waves. *J. Mar. Sci. Eng.* **2023**, *11*, 1913. [CrossRef]
3. Sun, L.; Yang, X.-Q.; Bu, S.-X.; Zheng, W.-T.; Ma, Y.-X.; Jiao, Z.-L. Analysis of FPSO Motion Response under Different Wave Spectra. *J. Mar. Sci. Eng.* **2023**, *11*, 1467. [CrossRef]
4. Li, B.; Zhang, X.; Wang, J.; Chen, N. Anti-Roll Characteristics of Marine Gyrostabilizer Based on Adaptive Control and Hydrodynamic Simulation. *J. Mar. Sci. Eng.* **2022**, *10*, 83. [CrossRef]
5. Jiguang, S.; Lihua, L.; Songtao, Z.; Jiming, W. Design and experimental investigation of a GA-based control strategy for a low-speed fin stabilizer. *Ocean Eng.* **2020**, *218*, 108234. [CrossRef]
6. Songtao, Z.; Peng, Z. L2-Gain Based Adaptive Robust Heel/Roll Reduction Control Using Fin Stabilizer during Ship Turns. *J. Mar. Sci. Eng.* **2021**, *9*, 89. [CrossRef]
7. Zhang, S.; Zhao, P.; Li, C.; Song, Z.; Liang, L. Study on the Accessibility Impact of Anti-Rolling Tank on the Offshore Wind O&M Gangway. *J. Mar. Sci. Eng.* **2023**, *11*, 848. [CrossRef]
8. Zhang, S.; Zhao, P.; Gui, M.; Liang, L. Wavelet Neural Network-Based Half-Period Predictive Roll-Reduction Control Using a Fin Stabilizer at Zero Speed. *J. Mar. Sci. Eng.* **2023**, *11*, 2205. [CrossRef]
9. Townsend, N.C.; Murphy, A.J.; Shenoi, R.A. A new active gyrostabiliser system for ride control of marine vehicles. *Ocean Eng.* **2007**, *34*, 1607–1617. [CrossRef]
10. Schlick, E.O. Device for Minimizing the Oscillatory Movements of Ships. U.S. Patent 769,493, 6 September 1904.
11. Sperry, E.A. Ships' Gyroscopes. U.S. Patent 1,150,31, 2 August 1915.
12. Gillmer, R. *Modern Ship Design*; United States Naval Institute: Annapolis, MD, USA, 1984.
13. Palraj, M.; Rajamanickam, P. Motion control studies of a barge mounted offshore dynamic wind turbine using gyrostabilizer. *Ocean Eng.* **2021**, *237*, 109578. [CrossRef]
14. Hu, L.; Zhang, M.; Yu, X.; Yuan, Z.M.; Li, W. Real-time control of ship's roll motion with gyrostabilisers. *Ocean Eng.* **2023**, *285*, 115348. [CrossRef]

15. Li, J.Y.; Li, Y.S.; Chen, D.J.; Han, R.X.; Zhu, Z.J.; Zhang, J.X.; Du, Y.Z. A Fluid Momentum Wheel Roll Reduction Capability Verification System and Method. Patent CN115452347A, 9 December 2022.
16. Maynard, R.S. Fluid Momentum Control. U.S. Patent 4,776,541, 11 October 1988.
17. Kelly, A.; Mcchesney, C.; Smith, P. A performance test of a fluidic momentum controller in three axes. *NASA Rep.* **2004**.
18. Du, Y.Z.; Hou, C.G.; Xie, H.W.; Wang, L.L.; Wang, L.; Yang, Y.; Han, R.X. An Offshore Stabilized Platform Based on Circulation Momentum Moment Reduction Roll. Patent CN113562132B, 26 July 2022.
19. Wang, W.-h.; Zhang, K.-d.; Zheng, R.-s.; Wang, L.-l.; Du, Y.-z.; Huang, Y. Experimental and numerical analysis on the characteristics of flow field and precession moment in fluid momentum wheel with driven pump. *Ocean Eng.* **2024**, *293*, 116731. [CrossRef]
20. Dean, W.R. LXXII The stream-line motion of fluid in a curved pipe (Second paper). *Lond. Edinb. Dublin Philos. Mag. J. Sci.* **1928**, *5*, 673–695. [CrossRef]
21. Kalpakli Vester, A.; Orlu, R.; Alfredsson, P.H. Turbulent flows in curved pipes: Recent advances in experiments and simulations. *Appl. Mech. Rev.* **2016**, *68*, 050802. [CrossRef]
22. Di Piazza, I.; Ciofalo, M. Numerical prediction of turbulent flow and heat transfer in helically coiled pipes. *Int. J. Therm. Sci.* **2010**, *49*, 653–663. [CrossRef]
23. Canton, J.; Schlatter, P.; Örlü, R. Modal instability of the flow in a toroidal pipe. *J. Fluid Mech.* **2016**, *792*, 894–909. [CrossRef]
24. Cox, C.; Plesniak, M.W. The effect of entrance flow development on vortex formation and wall shear stress in a curved artery model. *Phys. Fluids* **2021**, *33*, 101908. [CrossRef]
25. White, C.M. Stream line flow through curved pipes. *Proc. R. Soc. Lond. A* **1929**, *123*, 645–663.
26. Ito, H. Friction factors for turbulent flow in curved pipes. *J. Basic Eng.* **1959**, *81*, 123–132. [CrossRef]
27. El-Genk, M.S.; Schriener, T.M. A Review and Correlations for Convection Heat Transfer and Pressure Losses in Toroidal and Helically Coiled Tubes. *Heat Transf. Eng.* **2017**, *38*, 447–474. [CrossRef]
28. Najjari, M.R.; Plesniak, M.W. Secondary flow vortical structures in a 180° elastic curved vessel with torsion under steady and pulsatile inflow conditions. *Phys. Rev. Fluids* **2018**, *3*, 013101. [CrossRef]
29. Rütten, F.; Schröder, W.; Meinke, M. Large-eddy simulation of low frequency oscillations of the Dean vortices in turbulent pipe bend flows. *Phys. Fluids* **2005**, *17*, 035107. [CrossRef]
30. Sudo, K.; Sumida, M.; Hibara, H. Experimental investigation on turbulent flow in a circular-sectioned 90-degree bend. *Exp. Fluids* **1998**, *25*, 42–49. [CrossRef]
31. Kim, J.; Yadav, M.; Kim, S. Characteristics of secondary flow induced by 90-degree elbow in turbulent pipe flow. *Eng. Appl. Comput. Fluid Mech.* **2014**, *8*, 229–239. [CrossRef]
32. Ikarashi, Y.; Uno, T.; Yamagata, T.; Fujisawa, N. Influence of elbow curvature on flow and turbulence structure through a 90° elbow. *Nucl. Eng. Des.* **2018**, *339*, 181–193. [CrossRef]
33. Kühnen, J.; Schwegel, M.; Hof, B.; Kuhlmann, H.C. Experimental investigation of the influence of curvature on transition to turbulence in a pipe. In Proceedings of the ETC 2013—14th European Turbulence Conference, Lyon, France, 31 May 2013.
34. Najjari, M.R.; Cox, C.; Plesniak, M.W. Formation and interaction of multiple secondary flow vortical structures in a curved pipe: Transient and oscillatory flows. *J. Fluid Mech.* **2019**, *876*, 481–526. [CrossRef]
35. Hellström, L.H.O.; Zlatinov, M.B.; Cao, G.; Smits, A.J. Turbulent pipe flow downstream of a 90° bend. *J. Fluid Mech.* **2013**, *735*, R7. [CrossRef]
36. Noorani, A.; El Khoury, G.K.; Schlatter, P. Evolution of turbulence characteristics from straight to curved pipes. *Int. J. Heat Fluid Flow* **2013**, *41*, 16–26. [CrossRef]
37. Noorani, A.; Schlatter, P. Swirl-switching phenomenon in turbulent flow through toroidal pipes. *Int. J. Heat Fluid Flow* **2016**, *61*, 108–116. [CrossRef]
38. Wegt, S.; Maduta, R.; Kissing, J.; Hussong, J.; Jakirlić, S. LES-based vortical flow characterization in a 90°-turned pipe bend. *Comput. Fluids* **2022**, *240*, 105418. [CrossRef]
39. He, X.; Apte, S.V.; Karra, S.K.; Doğan, Ö.N. An les study of secondary motion and wall shear stresses in a pipe bend. *Phys. Fluids* **2021**, *33*, 115102. [CrossRef]
40. Menter, F.R.; Kuntz, M.; Langtry, R. Ten years of industrial experience with the SST turbulence model. *Heat Mass Transf.* **2003**, *4*, 625–632.
41. Zhang, K.D.; Wang, W.H.; Pan, K.Y.; Du, Y.Z.; Dan, Y.W.; Huang, Y. Essential analysis and quantitative evaluation on mechanical-energy loss of fluid momentum wheel. *Ocean Eng.* **2023**, *285*, 115321. [CrossRef]